

"This document is the unedited Author's version of a Submitted Work that was subsequently accepted for publication in the Journal of the American Chemical Society, copyright American Chemical Society after peer review. To access the final edited and published work see [https://pubs.acs.org/doi/10.1021/jacs.2c13437, see ACS Articles on Request]."

Alloying as a Strategy to Boost the Stability of Copper Nanocatalysts during the Electrochemical CO₂ Reduction Reaction.

Valery Okatenko, Anna Loiudice, Mark A. Newton, Dragos C. Stoian, Anastasia Blokhina, Alexander N. Chen, Kevin Rossi, Raffaella Buonsanti*

*email: raffaella.buonsanti@epfl.ch

ABSTRACT

Copper nanocatalysts are among the most promising candidates to drive the electrochemical CO₂ reduction reaction (CO₂RR). However, the stability of such catalysts during operation remains sub-optimal, and improving this aspect of catalyst behavior remains a challenge. Here, we synthesize well-defined and tunable CuGa nanoparticles (NPs) and demonstrate that alloying Cu with Ga considerably improves the stability of the nanocatalysts. In particular, we discover that CuGa NPs containing 17 at. % of Ga preserve most of their CO₂RR activity for at least 20 hours while Cu NPs of the same size reconstruct and lose their CO₂RR activity within 2 hours. Various characterization techniques, including X-Ray photoelectron spectroscopy and *operando* X-Ray absorption spectroscopy, suggest that the addition of Ga suppresses Cu oxidation at open circuit potential (ocp), and induces significant electronic interactions between Ga and Cu. Thus, we explain the observed stabilization of the Cu by Ga as a result of the higher oxophilicity and lower electronegativity of Ga, which reduce the propensity of Cu to oxidize at ocp and enhance bond strength in the alloyed nanocatalysts. In addition to addressing one of the major challenges in CO₂RR, this study proposes a strategy to generate nanoparticles which are stable under a reducing reaction environment.

INTRODUCTION

The electrochemical CO₂ reduction reaction (CO₂RR) is a promising route towards closing the carbon cycle by converting CO₂ into key chemicals and fuels while storing renewable energy.¹ Cu-based materials are the most utilized catalysts for this reaction when the goal is the production of beyond-CO compounds, including hydrocarbons and alcohols.¹ While polycrystalline Cu foil produces more than sixteen different products, tuning the morphology and the size of Cu nanoparticles (NPs) enhances selectivity and activity towards one reaction product, for example methane, ethylene or ethanol.¹⁻³ Unfortunately, the operational stability of Cu NPs is limited, as these materials undergo reconstruction during CO₂RR.⁴⁻⁸ In particular, the reconstruction of Cu NPs is associated with Cu dissolution and reprecipitation which results in the formation of small clusters and agglomeration.⁴⁻⁷ Surface oxidation at open circuit potential (ocp) accounts for the initial dissolution which continues during operation mediated by soluble Cu intermediate species, whose chemical nature has not yet been identified.⁸

In the current literature, strategies to mitigate the reconstruction of Cu NPs during CO₂RR are scarce. Carbon shells might provide a physical barrier against dissolution; however the NPs must be stable under the often harsh conditions used for the synthesis of these coatings (e.g. high temperature required for the carbonization of organic layers).⁹⁻¹¹ Studies in oxygen electrocatalysis have proved that the alloying of Pt, Pd and Ir NPs with guest elements dramatically improves the stability of these NPs against dissolution during catalysis by virtue of effects which span from the increase in the metal oxidation potential to sacrificial dissolution of the less noble metals.¹²⁻¹⁸ For example, Zhang et al. report that Au clusters deposited on the surface of Pt NPs enhance the stability of Pt as an oxygen reduction reaction catalyst because the *d*-band interactions between Au and Pt increase the oxidation potential of Pt.¹² In another study, a Pd overlayer on the surface of Au NPs was demonstrated to be more resilient to dissolution than pure Pd NPs because of the Au – Pd bond being stronger compared to the Pd – Pd bond.¹³ Cu-based alloyed NPs are currently investigated as CO₂RR catalysts; however, these studies mostly focus on tuning the selectivity rather than aiming at developing guidelines towards increasing the performance stability of the Cu NPs.^{2,19-23} Based on the current knowledge regarding the reconstruction of Cu in CO₂RR, and inspired by the studies on oxygen electrocatalysis, we hypothesize that the combination of Cu with an element M which possesses a higher oxophilicity and lower electronegativity than Cu should reduce the tendency of Cu to oxidize at ocp and form heteroatomic Cu – M bonds with higher dissociation energies than Cu – Cu, which should further hamper Cu dissolution and thus improve the performance stability of Cu NPs during CO₂RR.

In this work, we synthesize CuGa alloy NPs with tunable composition and characterize them as CO₂RR electrocatalysts with the aim of testing this hypothesis. Among various guest elements, calculations have proposed Ga to enhance the CO₂RR activity of Cu.^{24,25} Furthermore, Ga does match the criteria listed above, namely that Ga is more oxophilic than Cu, and the Cu – Ga bond energy is greater than either Cu – Cu or Ga – Ga.^{26,27} We use colloidal synthesis to prepare CuGa NPs with a narrow size distribution and three different compositions (4 at. %, 17 at. % and 37 at. % of Ga content). We show that alloying Cu with Ga greatly improves the stability of the catalyst. Specifically, we find an interesting non-monotonic dependence in the stability trend with the sample containing 17 at. % of Ga being the most stable among the tested compositions. We use a combination of electrochemistry, electron microscopy, density functional theory calculations and X-Ray spectroscopy, including *operando* X-Ray absorption, to explain the increased stability of the CuGa NPs which we correlate to the suppressed Cu oxidation at ocp, charge redistribution between Ga and Cu, and the metallic bond strengthening in the lattice.

EXPERIMENTAL SECTION

Chemicals

Tris(dimethylamido)gallium (III) dimer (Ga₂(NMe₂)₆, 99.9 %) was purchased from ABCR. Copper (I) bromide (99 %), trioctylphosphine oxide (C₂₄H₅₁PO or TOPO, 99 %), oleylamine (C₁₈H₃₅NH₂ or OLAM, 70 %), 1-octadecene (C₁₈H₃₆ or ODE, 90 %), toluene (anhydrous, 99.8 %) and ethanol (anhydrous, 99.5 %) were purchased from Sigma-Aldrich. Hexane (anhydrous, >96 %) was bought from TCI Chemicals. Potassium carbonate (K₂CO₃, 99+ %, ACS reagent) was obtained from Acros organics. ODE was degassed under vacuum at 110 °C for 4 h, cooled to room temperature, and then transferred in an airtight manner to the glove box. All syntheses were carried out under an inert atmosphere using anhydrous solvents and standard glovebox and Schlenk-line techniques. NPs washing, handling, and storage were also carried out under inert atmosphere.

NP Synthesis

Cu NPs. Cu NPs were synthesised by modifying the procedure reported by Loiudice et al.²⁸ 0.7 g of TOPO was added to 11.5 ml of OLAM in a three-necked round bottom flask and degassed for at least 30 minutes under strong magnetic stirring, during which time the TOPO dissolves in the OLAM and the solution turns colorless. The Cu precursor solution was prepared by dissolving 50 mg of CuBr in the 5 ml of degassed TOPO and OLAM. This solution was heated for 15 min at 80 °C in the glovebox to dissolve TOPO and CuBr. Then, the Cu

precursor solution was transferred to the three-necked flask with a syringe to avoid oxidation. After that, the reaction mixture was brought to the temperature of 260°C under N₂-flow and left at this temperature for 60 min. As a result, reddish-brown solution is formed. The heating was then removed and the flask was allowed to cool to 90°C. The solution was transferred to the glovebox and washed once with anhydrous hexane (1 : 1 hexane to reaction mixture ratio) by centrifuging at 6000 rpm for 10 minutes. The supernatant was disposed of, and the precipitate recovered in degassed OLAM for further use as seeds, or in anhydrous toluene for the further use as electrocatalyst (with the final concentration of *ca.* 5 mg/mL).

CuGa NPs. CuGa NPs were synthesized according to a modified procedure based on Clarysse et al.²⁹ 15 mg of Cu NPs in oleylamine were added to the three-necked round bottom flask with 11.5 ml of degassed oleylamine. The solution was heated to 280°C under flowing N₂. This step was followed by the hot-injection of a Ga-precursor, prepared by dissolving 17, 35 or 70 mg of Ga₂(NMe₂)₆ in 3 ml of degassed ODE to obtain CuGa4, CuGa17 and CuGa37 samples, respectively. After the hot injection, the reaction solution was kept at a temperature of 280°C for 1 hour, and allowed to cool to room temperature. The solution was transferred to the glovebox and washed once with anhydrous hexane (1 : 1 hexane to reaction mixture ratio) by centrifuging at 6000 rpm for 10 minutes. After that, the supernatant was disposed of, and the precipitate recovered in hexane. Ethanol was then added in 1 : 1 ratio, followed by centrifugation for 5 min at 6000 rpm. Finally, the supernatant was disposed of, and the CuGa nanoparticles were dispersed in 5 ml of toluene (with the final concentration of *ca.* 1 mg/mL).

Materials characterization

Powder X-Ray diffraction (XRD) patterns were acquired on a Bruker D8 Advance diffractometer with a Cu K α source equipped with a Lynxeye one-dimensional detector. The diffractometer operated at 40 kV and 40 mA with a Cu K α source with wavelength of 1.54 Å.

Bright-field transmission electron microscopy (TEM) images of Cu and CuGa NPs were acquired on a Thermo-Fisher Tecnai-Spirit at 120 kV. 10 μ L of as-synthesized NPs were drop-casted on a carbon coated copper TEM grid (Ted Pella, Inc.) to prepare the sample for imaging. Particle size distribution was evaluated with the use of ImageJ software from datasets of 300 particles from three different images each.

High-angle annular dark field scanning transmission electron microscopy (HAADF-STEM) coupled with energy-dispersive X-ray spectroscopy (EDXS) was performed using a FEI Tecnai Osiris TEM in STEM mode with an accelerating voltage of 200 kV. The TEM was equipped with a high brightness XFEG gun and four windowless Super-X silicon drift detectors for EDS. Bruker Esprit was used for data analysis. To analyze the samples after CO₂RR, gold

TEM grid (Ted Pella, Inc.) was placed on the electrode inside the glovebox, 10 μ l of ethanol were placed on the area coated with the catalyst, and the catalyst film was gently scratched with the grid.

X-Ray photoelectron spectroscopy (XPS) and Auger spectroscopy analyses were performed by using an Axis Supra (Kratos Analytical) instrument using the monochromated $K\alpha$ X-ray line of an Al anode. The pass energy was set to 40 eV with a step size of 0.15 eV. The samples were electrically insulated from the sample holder, and charges were compensated. Cu and CuGa NP samples were prepared by drop-casting films onto clean glassy carbon substrates. The same substrates were used in electrochemical experiments. XPS fitting was performed in CasaXPS software. All data were referenced to the principal C 1s peak at 284.8 eV after fitting. In the Ga 2*p* region, only the Ga 2*p*_{3/2} peaks were used for fitting and quantification. In the Ga 3*d* region, both Ga-metal and Ga-oxide peaks were fitted with contributions from spin-orbit coupling; the Ga 3*d*_{3/2} and Ga 3*d*_{5/2} peak separations were fixed at 0.46 eV, and the relative intensities were fixed at 0.633. In the Cu 2*p* region the area under the peak at around 932.5 eV was used for the quantification. In general, all peaks from a particular region were first fitted with equal line widths, and then this constraint was relaxed to refine the fit.

The NPs solution concentration was determined by Inductively Coupled Plasma Optical Emission Spectrometry (ICP-OES) performed on an Agilent 5100 device with a VistaChip II CCD detector. Each sample aliquot (20 μ l) was first dried, then digested overnight in 142.5 μ L of 70 % HNO₃ ICP grade solution (Sigma-Aldrich) before being finally diluted with Milli-Q water to obtain the 2 wt. % acid content needed for the analysis. ICP grade Cu and Ga standard solutions (1000 ppm in 2 wt. % HNO₃) were diluted with 2 wt. % HNO₃ to get fresh standards before each analysis and to create the calibration plot employed to determine the concentration of the sample solutions.

Electrode preparation

Glassy carbon plates (2.5 cm \times 2.5 cm \times 0.3 cm, Sigradur G, HTW) coated with electrocatalyst were used as the working electrode. Before coating, the glassy carbon plates were cleaned by consecutive sonication (Bandelin Sonorex RK 106, 35 kHz) in acetone, isopropanol and water for 10 min each to remove adsorbed contaminants of different nature. After this, the glassy carbon plates were polished using an alumina paste (50 nm alumina, BAS Inc.) on a polishing pad. Then, the substrates were sonicated in Milli-Q water for another

10 min, polished again on the pad free of alumina to make sure that alumina was removed and, finally, the glassy carbon plate was blown dry with N₂.

The working electrodes (cathodes) were prepared by drop-casting 15 µg of Ga NPs in 14 µL of toluene onto a circular area of 1.33 cm² on the glassy carbon plates. No binder (e.g. Nafion) or carbon were added to the catalyst, as NP electrode films prepared as described do not detach from the electrode surface during the measurement and are sufficiently conductive on their own. After drop-casting, the electrodes were allowed to dry for 10-15 min, rinsed with ethanol to remove ligands, and with water to remove excess of ethanol. The electrodes were blown dry with N₂ and tested as-prepared.

Electrocatalytic measurements

All the electrochemical measurements were controlled with Biologic SP-300 potentiostat. Ambient pressure CO₂ electrolysis was carried out in a home-built, custom-made, gas-tight, electrochemical H-cell made of polycarbonate and fitted with Buna-N O-rings. In this electrochemical cell configuration, the working electrode and counter electrode are configured parallel to each other to ensure a uniform potential distribution across the surface. Both working and counter electrodes exposed geometric surface areas of 1.33 cm² limited by the O-rings. Catholyte and anolyte compartments were each filled with 2 mL electrolyte to concentrate liquid products and permit their detection. A Selemion AMV anion exchange membrane was used to separate the anodic and cathodic compartments and minimize reoxidation of CO₂RR products on the anode. Pt foil was used as the counter electrode, and Ag/AgCl electrode (leak free series) (Innovative Instruments, Inc.) was used as the reference electrode.

0.1 M KHCO₃ solution was used as electrolyte. To prepare such solution, 0.276 g of K₂CO₃ were diluted in 40 mL of Milli-Q water to obtain 0.05 M K₂CO₃ solution, which was bubbled for 30 min with CO₂ (99.999 %, Carbagas) prior to the start of measurements. During electrolysis, CO₂ was pre-humidified by flowing through a water bubbler, and constantly supplied to both cell compartments via custom-made ceramic frits at a flow rate of 5 sccm each. With this, the gas was bubbled through the electrolyte to prevent CO₂ depletion, as well as to allow continuous analysis of gaseous products via a gas chromatograph. A mass flow controller (Bronkhorst) was used to control the flow rate of CO₂. For the experiments under N₂ atmosphere, the only difference was the gas source (N₂, 99.999 %, Carbagas); all the other details remained the same. The electrolysis experiments were performed in chronoamperometry mode.

Electrochemical impedance spectroscopy (EIS) was implemented prior to the main chronoamperometry measurement to determine the electrochemical cell resistance (R_{cell}) and compensate for the ohmic losses. Four spectra were measured at the open-circuit potential, using 41 points between 1 MHz and 100 Hz, using a sinus amplitude of 20 mV and a pause time of 0.6 s between each frequency. Software in-built into the potentiostat software (EC-lab) was used to apply the ohmic loss correction to further measurement.

Products analysis

Gas chromatograph (GC, SRI instruments) equipped with a HayeSep D porous polymer column, thermal conductivity detector and flame ionization detector was used for the analysis of gaseous products. The GC was calibrated for H_2 , CO , CH_4 , C_2H_4 and C_2H_6 . Five standard gas mixtures (Carbagas) were used to obtain the calibration plots for gaseous products concentrations determination. Ultra-high purity N_2 (99.999 %) was used as a carrier gas.

The Faradaic efficiency for the gaseous products is calculated with the following equation:

$$FE = \frac{n_e \times F \times C \times f \times P}{R \times T \times I}$$

where n_e is the number of electrons transferred to product formation; F is the Faraday constant (96485 C mol^{-1}); C is the measured concentration of the product by GC (in ppm); f is the gas flow rate (mL s^{-1}); P is the pressure ($1.01 \times 10^5 \text{ Pa}$); I is the imposed current (in A); R is the universal gas constant ($8.314 \text{ J mol}^{-1} \text{ K}^{-1}$) and T is the temperature (K). Values obtained after 10 min of electrolysis are not included in the calculation of Faradaic efficiency, as the GC gas flow is not yet stabilized at that point.

The Faradaic efficiency of liquid products was determined in a similar manner. 0.25 mL of both the catholyte and the anolyte were collected and analyzed with high-performance liquid chromatography (HPLC) on UltiMate 3000 instrument from Thermo Scientific, which is equipped with Refractive Index Detector for products quantification and Aminex HPX-87H (BioRad) column for products separation (1 mM H_2SO_4 was used as eluent). The necessity to collect electrolyte from both compartments is reasoned by the possible products crossover from the catholyte to the anolyte compartment.

The resulting formula used for calculations of liquid products' FE is:

$$FE = \frac{n_e \times F \times C}{V \times I \times t}$$

where n_e is the number of electrons transferred to product formation; F is the Faraday constant; C is the measured concentration of the product by HPLC (mol mL^{-1}); V is the cell volume (4 mL); I is the measured current (A); t is the duration of electrolysis (3600 s).

The electrode potential is recalculated with respect to RHE reference using iR compensation according to the equation:

$$E_{RHE} = E_{Ref} + 0.206 + 0.0591 \times pH - (R_{cell} \times I)$$

where E_{Ref} is the recorded potential against the Ag/AgCl reference electrode (V); +0.206 V is the Ag/AgCl reference electrode correction; R_{cell} is the ohmic resistance between the working and the reference electrode, which was defined using electrochemical impedance spectroscopy analysis prior to the measurement (Ohm); I is the imposed current (A).

For all values, error bars, representing standard deviations obtained with triplicate measurements, are given.

***Operando* X-Ray absorption spectroscopy**

Operando X-Ray absorption spectroscopy (XAS) measurements, at both Cu K- and Ga K-edges, were made in fluorescence mode at BM31 of the Swiss-Norwegian beamlines at the ESRF, Grenoble, France.³⁰ A Si(111) double crystal monochromator, and a Vortex[®] single-element Si drift fluorescence detector with XIA-Mercury digital electronics were used. The X-ray beam was applied in an unfocused state and shaped to ca. 3 mm (horizontal) and 0.5 mm (vertical) via the uses of slits.

The samples were drop-casted onto polished glassy carbon electrodes equivalent to the ones used in the lab based studies, except the smaller thickness in the case of the XAS studies (0.5 mm). The loading was increased to 60 μg to improve the signal-to-noise ratio. The prepared catalyst film on the electrode was then mounted in a custom-made electrochemical system the details of which may be found in earlier reports.^{31,32} The cell reproduces the same H-cell used in the lab experiments, but with a Kapton window in the back of working electrode to allow the X-rays to pass through to the sample and fluorescence X-rays detected. This way, the experiment environment was as close to the in-house electrochemical testing as possible to allow *operando* material characterization. To obtain the Cu reference spectra, Cu foil was used, along with Cu_2O and CuO powders diluted in boron nitride and shaped into the form of pellet. A metallic Ga film, obtained by exfoliation of warm Ga pellet with Kapton tape, and Ga_2O_3 powder diluted in boron nitride and shaped into the form of pellet, were used as references for the Ga K-edge. Other testing parameters were identical to those used in the lab-based tests.

Two types of measurement were made. Firstly, extended X-Ray absorption fine structure (EXAFS) was collected for both Cu K- and Ga K-edges for the catalysts at open-circuit conditions and *operando* at $-1.2 V_{\text{RHE}}$ in the chronoamperometric regime. Secondly, with the CO₂RR operation conditions applied, shorter and more rapid (ca. 2 mins per spectrum) X-Ray absorption near edge structure (XANES) data was collected, again at both Cu and then Ga K-edges. In all cases, the experimental conditions (CO₂ flow rate, electrolyte etc.) were kept identical to the lab-based tests.

XAS data processing and analysis

Data extraction, normalization, and averaging to obtain the heat maps of XAS spectra evolution during operation were performed using the Demeter package (Athena and Artemis).³³ In addition, the XAS data were reduced and normalized using the Prestoprnto package that was also subsequently used to perform linear combination analyses.³⁴ Subsequent analysis of the extracted EXAFS data was performed using EXCURV (v. 9.3).³⁵

RESULTS AND DISCUSSION

Catalyst synthesis and characterization

CuGa NPs were synthesized by following a previously reported seeded-growth method, where a Ga molecular precursor is injected into a flask containing pre-synthesized Cu NPs (i.e. the seeds) at 280 °C (**Figure 1A**).²⁹ CuGa NPs containing 4, 17 and 37 at % of Ga (further denoted as CuGa4, CuGa17 and CuGa37, respectively), as determined by the ICP-OES, were obtained by tuning the amount of Ga precursor during the synthesis (see Experimental section for details). TEM images of the Cu NPs used as seeds and of the as-synthesized CuGa NPs are reported in **Figure 1B-E**. These images show that all the NPs have same morphology and similar size between 40 nm and 50 nm with 10 % standard deviation within each sample (**Figure S1**). The XRD characterization in **Figure 1F** reveals that CuGa4 and CuGa17 are crystallized with the same Cu-based *fcc* lattice as the only crystalline phase. The shift of the (111) and (200) peaks to lower 2θ values is consistent with the incorporation of increasing Ga content in the Cu lattice, according to the Vegard's law. Ga has a greater atomic radius than Cu and thus increases the interplane distances and unit cell parameter as it is included in the lattice. By contrast, the CuGa37 consists mostly of the Cu₉Ga₄-type primitive cubic lattice, with a minor contribution from an *fcc* Ga-rich phase, in agreement with other reports.^{36,37}

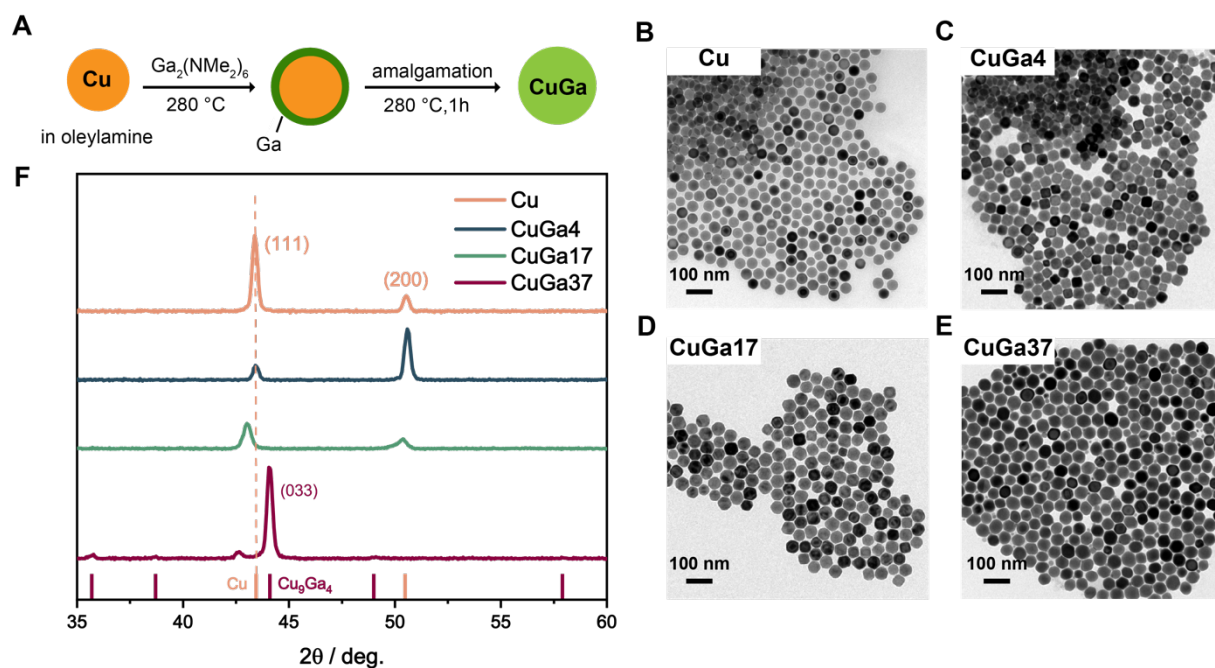


Figure 1. Synthesis and characterization of CuGa NPs. (A) Simplified synthetic scheme; (B-E) Bright field TEM of (B) Cu, (C) CuGa4, (D) CuGa17 and (E) CuGa37 NPs; (F) corresponding XRD patterns. These data indicate that CuGa NPs with the same morphology, very similar size and different Ga content were synthesized.

CO₂RR performance

Having synthesized well-defined CuGa NPs with tunable composition, we proceeded to test their behavior as CO₂RR electrocatalysts (**Figures 2, 3, S2 – S9**). We selected the Cu NPs, used as seeds for the synthesis of the CuGa NPs, as the reference catalyst. We do not include the Ga NPs as they are liquid under the conditions required for testing, and therefore distinctly different from the solid alloy NPs; in terms of the selectivity, Ga NPs produce only H₂ and CO.³¹

Figure 2A reports the Faradaic efficiency (FE, left axis) of all samples averaged over 45 minutes of chronoamperometry at different voltages, together with the corresponding total geometric current density (j , right axis; j vs. time graphs are reported in **Figure S2**). The addition of Ga to Cu suppresses the production of ethylene and promotes methane across the entire potential range, which becomes more evident when looking at the $FE_{CH_4}/FE_{C_2H_4}$ reported in **Figure 2B**. CuGa17 reaches the highest FE_{CH_4} of 52 % at -1.2 V_{RHE}. In absolute numbers, CH₄ accounts for 72 mol.% of all CO₂RR products (including liquids) and 90 mol.% of the CO₂RR gaseous products (namely, CO, CH₄ and C₂H₄) (**Figure S3**), which is a more significant number from the perspective of product separation as liquids and gases go towards

different product streams. We note that potentials more positive than $-1.0 V_{\text{RHE}}$ generate mostly hydrogen from the competing hydrogen evolution reaction (HER). Detection of small amounts of CO_2RR products at low overpotentials was also reported.³⁸ From a mechanistic perspective, one way to rationalize the methane promotion by addition of Ga to Cu is to consider the higher oxophilicity of Ga which favours the CO protonation and stabilizes the key methane intermediate $^*\text{COH}$.^{32,39,40} Indeed, density-functional theory (DFT) calculation of $^*\text{CO}$ protonation energy, which is the primary CH_4 selectivity descriptor,^{41,42} supports this hypothesis (**Figures S4, S5**), with a volcano-type dependence from Cu to CuGa37 peaking at CuGa17. Along with CH_4 , HER is promoted as the Ga amount increases, which is reasonable considering that Ga alone generates CO and H_2 .^{31,43} As for the activity, j indicates that the addition of Ga promotes the overall product generation rate at potentials more negative than $-1.2 V_{\text{RHE}}$ which correlates with an increase of the electrochemically active surface area (ECSA) (**Table S1, Figures S6, S7**).

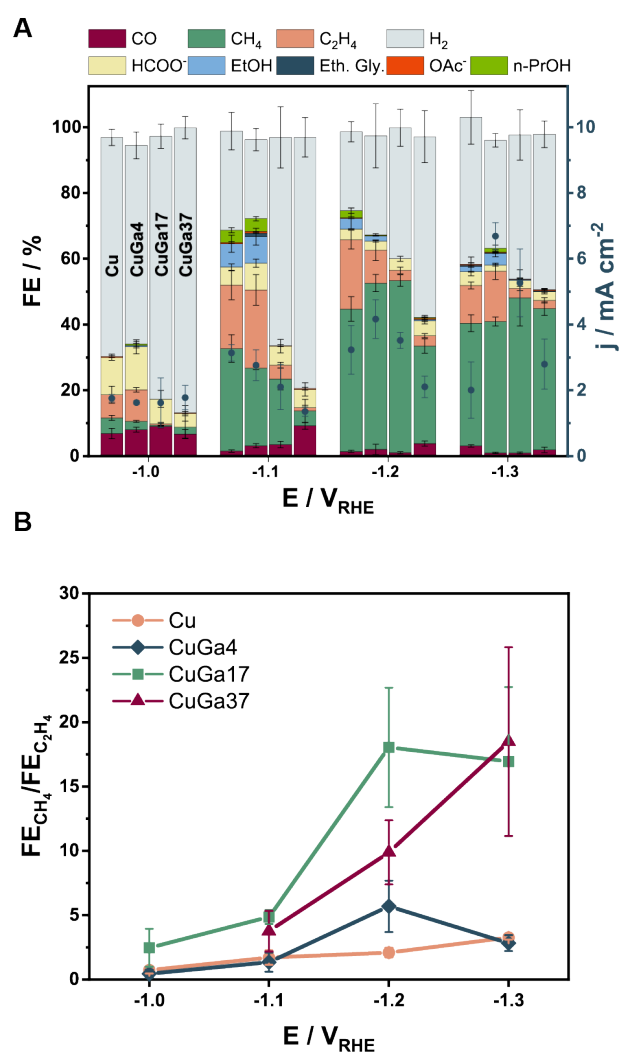


Figure 2. Performance of the CuGa NPs as CO₂RR electrocatalysts. (A) Average FE (left axis) and geometric current density (right axis) for Cu, CuGa4, CuGa17 and CuGa37 NPs during 45 min CO₂RR in CO₂-saturated 0.1 M KHCO₃ at different applied potentials (the NP loading was kept constant at 15 μg on glassy carbon with geometric area of 1.33 cm²). (B) Ratio of the FE for CH₄ and C₂H₄ over the same potential range, which indicates the CH₄ promotion in the CuGa NPs.

Having assessed the potential-dependent product distribution of the newly synthesized catalysts, we selected -1.2 V_{RHE} as the most representative voltage for stability tests with 4 hours as the initial monitoring time. **Figure 3** reports an overview of the obtained results. The performance of the Cu NPs deteriorate within the first 2 hours of electrolysis, meaning that the partial current densities corresponding to the CO₂RR products drops to zero. The addition of Ga clearly improves the CO₂RR current stability. Specifically, CuGa4 significantly stabilizes the CH₄ partial current density with around 50% of initial value being retained after 4 h test, which is remarkable considering the small % Ga in the sample. With further Ga addition (CuGa17), the catalyst performance become even more stable, with more than 90% of initial CH₄ partial current density retained after 4 h test. Strikingly, CuGa37 is less stable than CuGa4 and CuGa17. Longer testing, over 20 hours, shows that the CuGa17 still retains half of its initial j_{CH_4} , and that its overall CH₄ production over this extended timescale surpasses that of Cu by *ca.* 12 times thanks to the improved stability (**Figures S8, S9**).

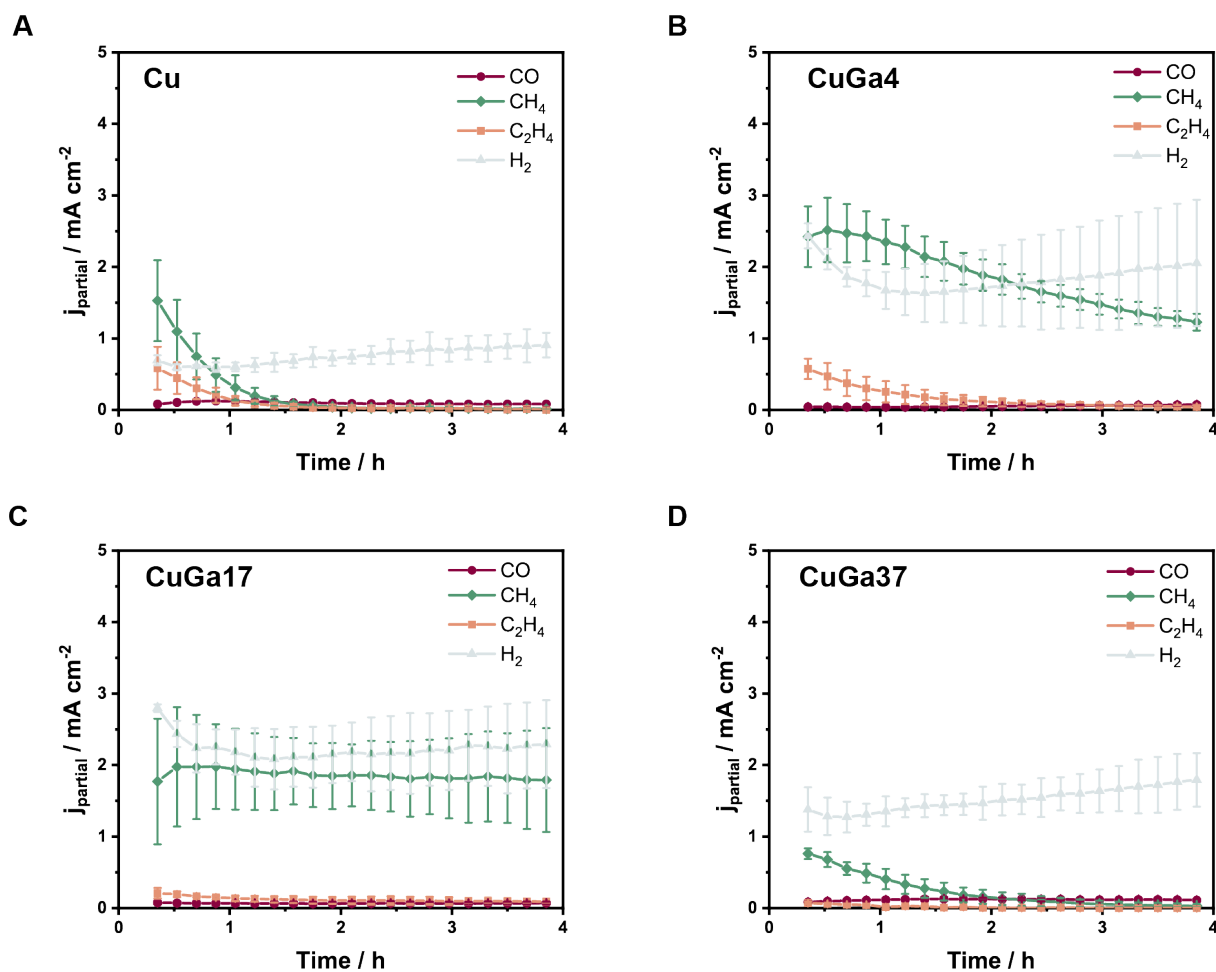


Figure 3. CO₂RR performance over time. (A-D) Partial current densities corresponding to the main gas products (i.e. H₂, CO, CH₄, C₂H₄) monitored over time for (A) Cu, (B) CuGa4, (C) CuGa17 and (D) CuGa37 NPs during 4 h of CO₂RR at -1.2 V_{RHE} in CO₂-saturated 0.1 M KHCO₃. These results indicate the superior operational stability of the CuGa NPs compared to the Cu NPs according to the following trend CuGa17 > CuGa4 > CuGa37 > Cu.

Compositional and structural characterization of the catalysts before and after CO₂RR

To gain more insight into the observed changes in stability, we performed different characterization techniques, including STEM and STEM-EDXS, selected area electron diffraction (SAED) and XPS before and after CO₂RR.

Figure 4 and **Figure 5** summarize the results obtained from STEM and STEM-EDXS. We characterized the catalysts after 1 hour, which is the time when Cu loses most of its activity while all the CuGa samples still maintain theirs to varying degrees, and after 4 hours, which is the time when CuGa4 and CuGa37 undergo significant decrease of current density while CuGa17 still preserves its electrocatalytic performance. In bimetallic catalysts, both

morphology and composition play a key role in governing the stability of catalytic performance.^{22,44,45} Thus, the following paragraphs discuss changes in both factors, while keeping in mind that deconvoluting the two is not trivial.

After 1 h of CO₂RR, the morphology of Cu clearly changes, resulting in the formation of NPs with undefined shape (**Figure 4**). Inductively coupled plasma – mass spectroscopy (ICP-MS) of electrolyte indicates that there is no significant dissolution of Cu into electrolyte (the Cu signal corresponds to < 1 % of total loading in all samples), which is consistent with previous data correlating the morphological changes to dissolution and redeposition of copper.⁸ On the contrary, all the CuGa NPs maintain their morphology after 1 h of CO₂RR (**Figure 4**). Notable differences between the CuGa samples emerge after 4 hours of CO₂RR. Indeed, the CuGa4 evolves into hollow NPs which resemble the reference Cu NPs after 1 h of operation, the CuGa17 does not show any change in its morphology, while significant surface roughening becomes evident for CuGa37.

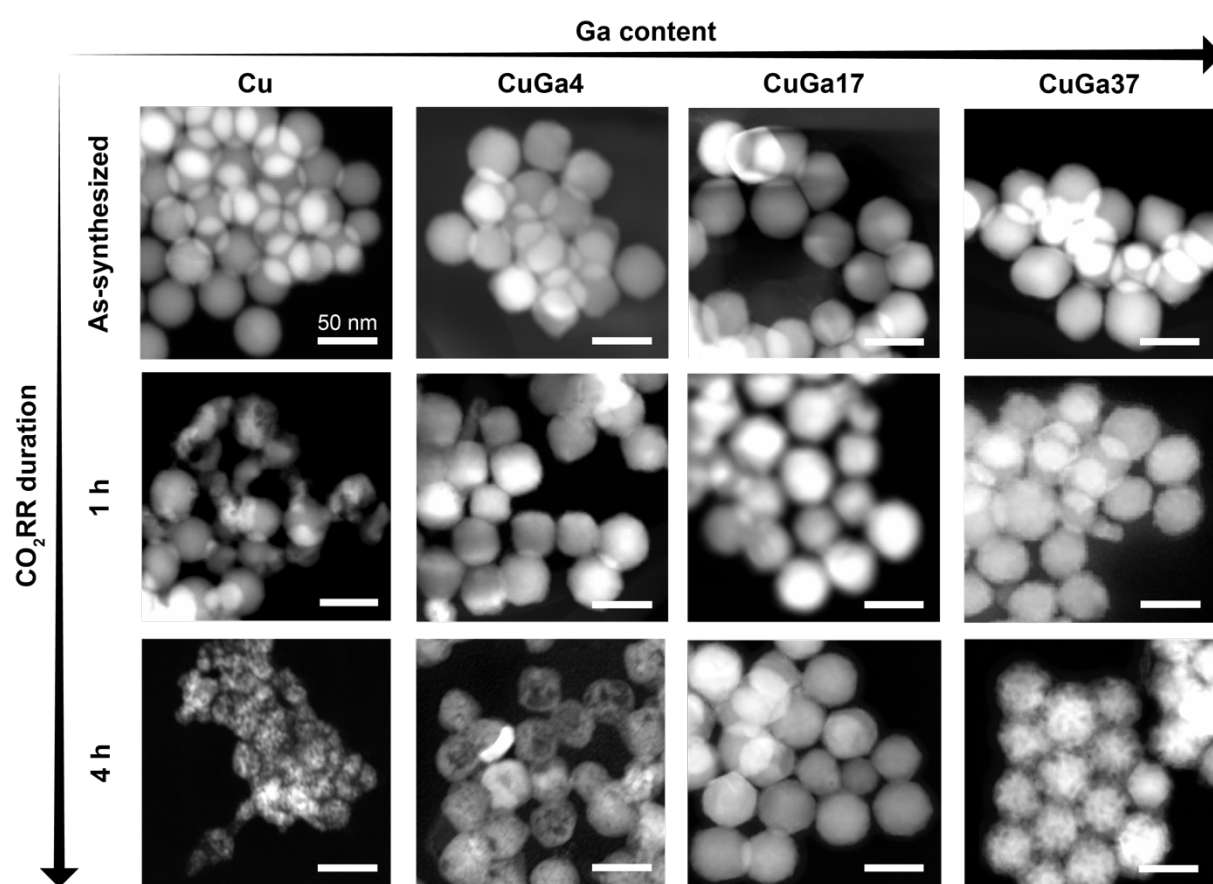


Figure 4. Morphological characterization of the NPs after CO₂RR. STEM images of Cu, CuGa4, CuGa17 and CuGa37 NPs in as-synthesized state and after 1 h and 4 h of CO₂RR

at $-1.2 V_{\text{RHE}}$. The scale bar is 50 nm. These data highlight a morphological stability of the NPs during CO_2RR according to the following trend $\text{CuGa17} > \text{CuGa4} \geq \text{CuGa37} \gg \text{Cu}$.

We used STEM-EDXS and line scans on single NPs to gain information on eventual changes in composition of the CuGaNPs (**Figure 5**). The data of the as-synthesized CuGa NPs indicate a homogeneous spatial distribution of the Ga and Cu signal within the NP core, which is consistent with the XRD data showing alloying of the two metals. Furthermore, the elemental content obtained from EDXS quantification of the entire imaged area, which is indicated on the top of the each image, is consistent with the values from ICP-OES. At the same time, Ga-rich shells are visible in all samples, most pronounced for the CuGa4 and CuGa17. The oxygen signal suggests an oxidized state of these shells (**Figure S10**), which can either form during the synthesis or subsequent exposure to air of the samples.

After 1 hour of CO_2RR , the Ga content decreases for all the samples. The most dramatic change in terms of relative at.% occurs for the CuGa4, although the EDX spectrum does confirm that Ga is still present in the sample (**Figure S11**). However, the absolute loss of Ga, which is around 5 at. % is similar for all the samples. Meanwhile, the STEM-EDXS mapping shows that the Ga-rich shells disappear for CuGa4 and CuGa17 while a slightly Cu-rich surface forms for CuGa37. After 4 hours of CO_2RR , no change in composition occurs. In terms of elemental distribution, additional Cu surface enrichment is observed in the line scans for CuGa37. A closer look at the NPs indicates that the features accounting for the surface roughness in the STEM correlate very well with the Cu signal (**Figure S12**).

ICP-MS of the electrolyte after 4 hours of CO_2RR shows that 2 – 4 % of catalyst mass loaded on the electrode dissolves, which is close to the Ga lost based on the STEM-EDXS quantification and suggests that the core alloy remains intact. In fact, the SAED patterns confirm that the phase of the NP core, after the 4 hours of CO_2RR , remains the same as the as-synthesized samples, namely *fcc* for Cu, CuGa4 and CuGa17 and Cu_9Ga_4 -type primitive cubic lattice for CuGa37 (**Figure S13**).

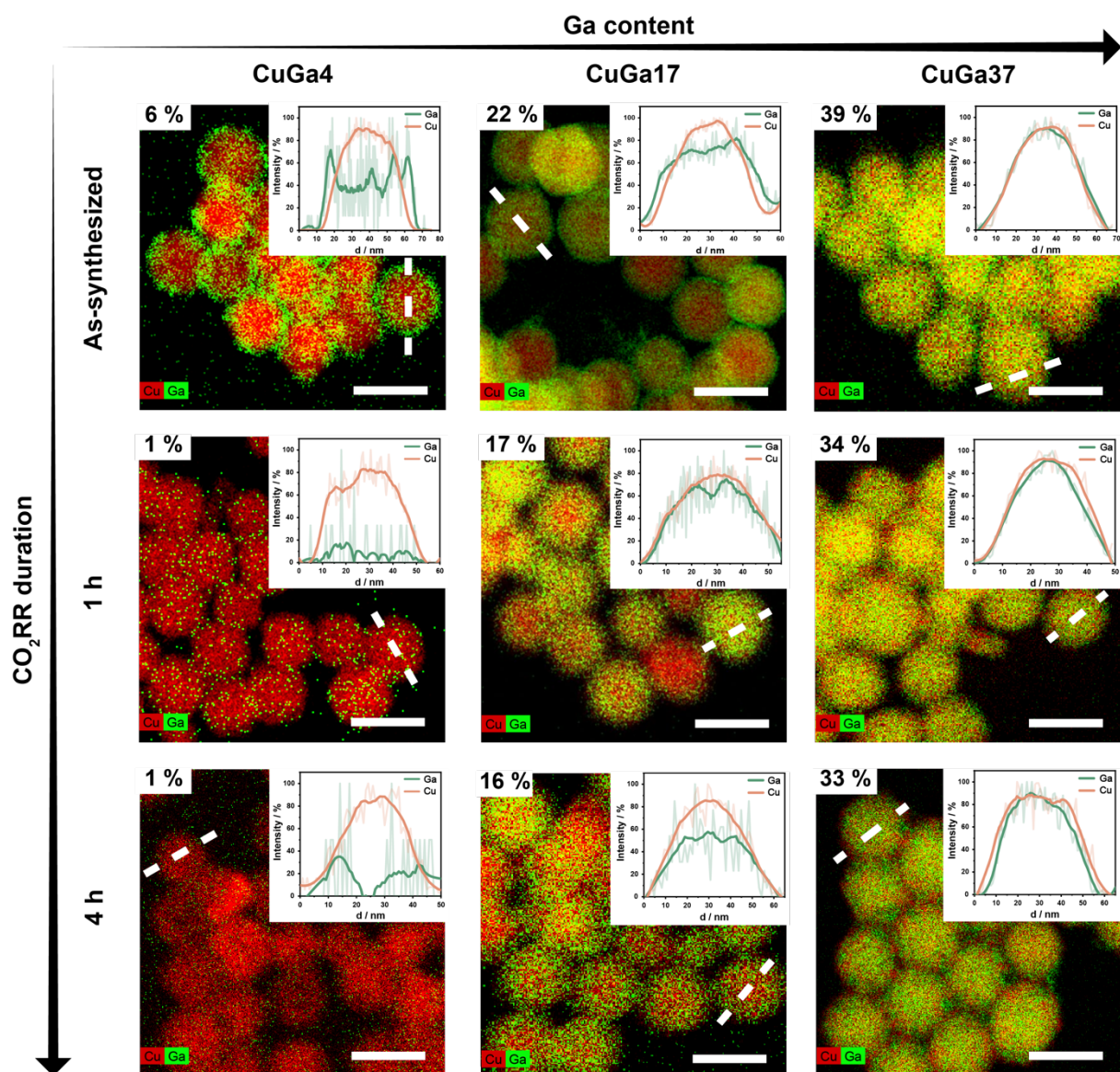


Figure 5. Composition and elemental distribution of the NPs after CO₂RR. STEM-EDXS elemental mapping (Cu – red, Ga – green) along with the line profile scan of one representative particle of CuGa₄, CuGa₁₇ and CuGa₃₇ NPs in as-synthesized state and after 1 h and 4 h of CO₂RR at -1.2 V_{RHE}. The scale bars are 50 nm. STEM-EDXS quantification results are reported on the top-left parts of the images (in at. %).

XPS was used as complementary characterization technique to gain insight into the surface composition of the as-synthesized CuGa NPs and of those after 4 h of CO₂RR (**Figure 6**).

Figure 6A reports the XPS data for the as-synthesized CuGa with different Ga content. The first panel shows the Ga 3*d* region, which was fitted with two components according to the literature.^{31,46–48} These two components are Ga₂O₃ and metallic Ga at higher and lower

binding energy, respectively. While the contribution of the oxide to the signal remains constant across the samples, the contribution of the metallic Ga increases with the Ga content. This observation is consistent with the higher Ga content in the NP core, which is presumably metallic, considering that the thickness of the Ga oxide shell is roughly 2 nm (**Figure S10**) and the X-Ray penetration depth is up to 6 nm for the Ga 3*d* region. Furthermore, the Ga peaks shift to the higher binding energy as the Ga content increases.

Interestingly, a similar shift is observed for the Cu 2*p* spectra shown in the second panel of **Figure 6A**. A convoluted effect arising both from the formation of an oxide/metal interface and from the bond strengthening between the metallic atoms due to alloying can account for these chemical shifts, which become more pronounced as the Ga content increases.

Finally, the Cu LMM Auger region in the third panel of **Figure 6A** provides information on the Cu oxidation state. The higher the Ga content is, the more metallic the Cu is, which suggests that the Ga-rich shell in CuGa₄ and CuGa₁₇ acts as protecting layer rendering the CuGa core less prone to oxidation at ambient conditions.

In addition, XPS quantification of the Ga content revealed an almost double amount of Ga content in all samples compared to the values obtained by EDXS quantification (**Figure S14**). Considering the XPS is a surface technique, these data confirms that the as-synthesized CuGa NPs consist of an alloyed CuGa core with a Ga-rich shell, which forms during the synthesis and oxidizes upon exposure to air and/or the electrolyte, in agreement with the STEM-EDXS data (**Figures 5, S10**).

We also carried out the same XPS analysis on the electrodes after 4 hours of CO₂RR, which is reported in **Figure 6B**. Please note that Ga 3*d* could not be used for this purpose, as potassium in the electrolyte deposits on the electrode during CO₂RR and the XPS signal of K 3*p* overlaps with the one of Ga 3*d* (washing the samples reduced the K 3*p* signal but did not remove it). Therefore, Ga 2*p* was used for the analysis. Because of the reduced penetration depth of the X-Ray in this energy range, only Ga oxide is detected in CuGa₁₇ and CuGa₃₇; the amount of Ga in CuGa₄ is probably below the detection limit. The chemical shift is still present both in the Ga 2*p* and in the Cu 2*p* post-CO₂RR in the samples with higher amount of Ga, which are CuGa₁₇ and CuGa₃₇. However, this shift is much smaller compared to that observed in the as-synthesized samples, which can be attributed to the fact that electric field effects due to the Ga oxide shell are no longer present and only effects due to alloying in the metallic state remain. Furthermore, the Cu LMM Auger peaks indicate that the oxidized Cu(I) is now present on the surface of all samples. Altogether, the post-CO₂RR XPS support the

hypothesis that the Ga-rich shells are removed during electrochemistry and that the only remaining Ga is the that bound in the bimetallic core.

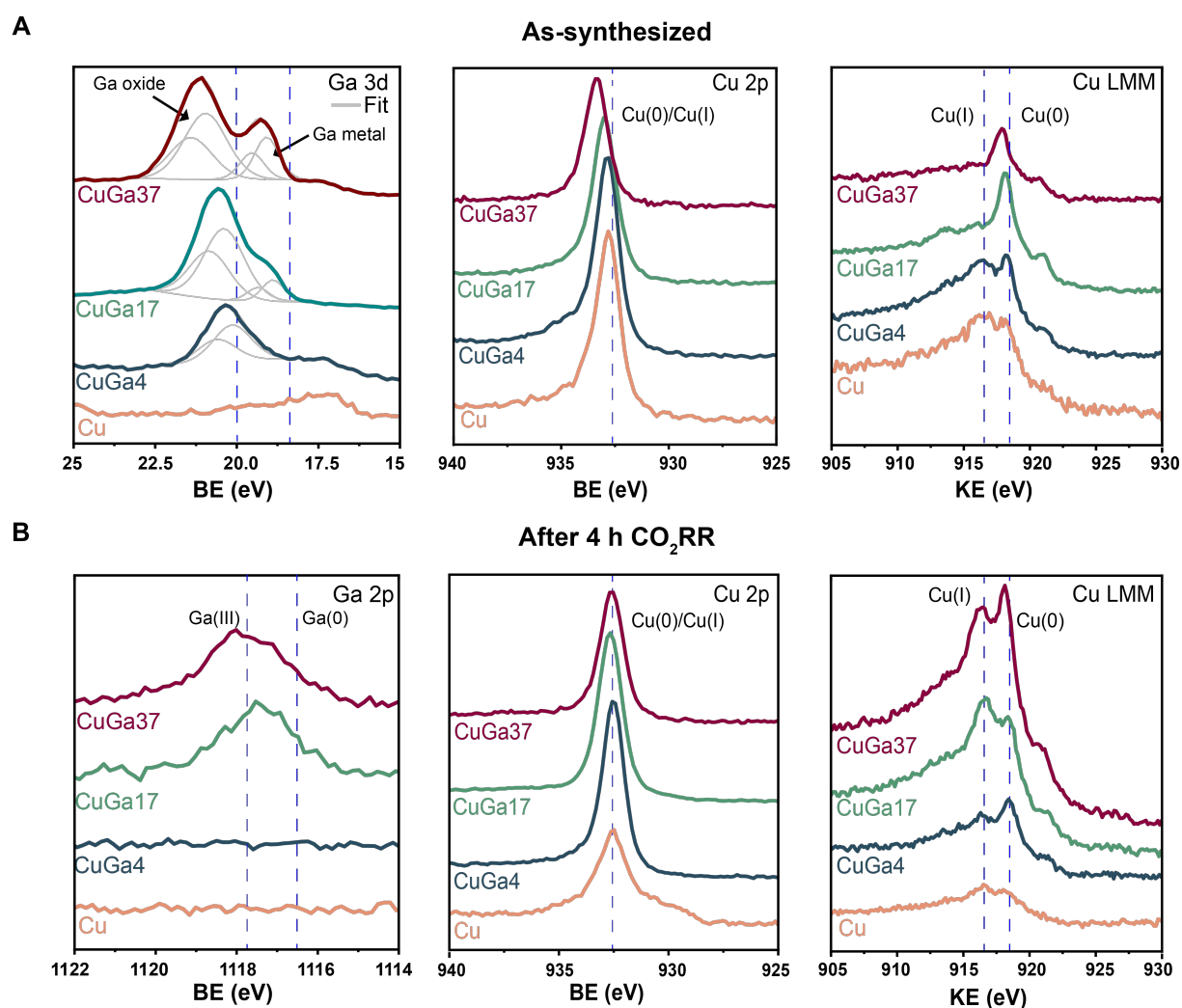


Figure 6. Surface analysis of the CuGa NPs before and after CO₂RR. (A) Ga 3*d*, Cu 2*p* XPS profiles and Cu LMM Auger spectra for the as-synthesized Cu, CuGa4, CuGa17 and CuGa37 NPs. (B) Ga 2*p*, Cu 2*p* XPS profiles and Cu LMM Auger spectra for the Cu, CuGa4, CuGa17 and CuGa37 NPs after 4 h of CO₂RR at -1.2 V_{RHE} in CO₂-saturated 0.1 M KHCO₃. Dashed lines indicate the reference positions of Ga 3*d*_{5/2}, Ga 2*p*_{3/2}, Cu 2*p*_{3/2} and Cu LMM peaks.^{49,50}

***Operando* X-Ray absorption characterization**

To gather complementary insight to those provided by the *ex situ* characterization, we performed *operando* XAS and monitored the catalyst state during electrolysis at $-1.2 V_{\text{RHE}}$. **Figure 7** and **Figures S15 – S29** report the XANES and EXAFS results for the Cu and CuGa NPs at ocp and during CO₂RR .

We note that the Ga K-edge signal for CuGa4 was too weak and noisy to yield any viable information (**Figure S15**). However, the data were sufficient to confirm that Ga is present on the electrode, supporting STEM-EDXS and XPS observations that Ga is present in this sample under operation despite its low *ca.* 1 % content. The Ga K-edge spectra of both CuGa17 and CuGa37 are characterized by a rising edge at *ca.* 10368 eV both at ocp (**Figure S16**) and during CO₂RR at $-1.2 V_{\text{RHE}}$ (**Figures 7A**), which indicate the presence of mostly metallic Ga. The temporal evolution maps (**Figure S17**) show that the application of the cathodic voltage slightly reduces the intensity of the Ga signal, in agreement with the observed loss of Ga in the STEM-EDXS and XPS data, which then remain stable during the next 3 hours of CO₂RR at $-1.2 V_{\text{RHE}}$. Because Ga is crystallized in the *fcc* (CuGa17) and Cu₉Ga₄-type (CuGa37) lattices for which there are no Ga and Ga₂O₃ standards, linear combination analysis (LCA) was not applicable for the quantification of the metallic and oxidized components in the Ga K-edge. However, the Ga K-edge XANES shape profiles qualitatively indicate that a minor fraction of Ga might still be oxidized under operation because of the features at *ca.* 10377 eV, most evident for CuGa17, which persist at $-1.2 V_{\text{RHE}}$.

The position and the shape profile of the Cu K-edge indicate that the Cu is mostly metallic at both ocp (**Figure S18**) and under cathodic potential (**Figure 7B**). A very rapid shift to lower energies compared to ocp is observed upon the application of the cathodic voltage in the temporal evolution maps (**Figure S19**), which is consistent with the reduction of an oxidized Cu₂O surface formed at ocp.^{8,51} No significant change follows during the next 3 hours of CO₂RR at $-1.2 V_{\text{RHE}}$.

LCA of the Cu XANES profiles provides the fraction of Cu₂O and metallic copper at ocp and at $-1.2V_{\text{RHE}}$ during CO₂RR in the different samples (**Figures 7C, S20**). The data at ocp indicate that the fraction of oxidic copper is significant for pure Cu and CuGa4, while it drops substantially for CuGa17. As the Cu₂O content obtained by the fitting for CuGa17 is not statistically different from zero, the LCA analysis suggests that surface oxidation is suppressed at ocp for this sample. LCA is not applicable for Cu in CuGa37, as there are no appropriate Cu and Cu₂O standards for the Cu₉Ga₄-type structure. Yet, the K-edge position qualitatively suggests that Cu is purely metallic. Altogether, the LCA analysis at ocp suggests that the Ga-

rich samples protect copper from oxidizing, consistent with deductions made from Auger spectroscopy carried out on the as-synthesized sample (**Figure 6A**).

Finally, one interesting observation in the XANES data is that the Cu and Ga K-edge positions follow a composition-dependent trend: as the content of Ga in the CuGa NPs increases, the Cu and Ga K-edge absorption edges shift to higher energies (**Figures 7D,E**). As this shift is not accompanied by the rise of Cu pre-edge feature at *ca.* 8981 eV, which is characteristic of Cu(I) presence, this increase cannot be attributed to the Cu oxidation upon increase in Ga content in the alloy. Instead, it may indicate an increasing binding energy of both metals in the lattice, which agrees with the observation made in the XPS data.

We gained further structural insight from the EXAFS spectra for Cu and Ga (**Figures 7F,G, S21-S29, Table 1**). The degree of structural order, which is one of the factors contributing to the intensity of the signal, follows a composition-dependent trend for both metals and decreases as the Ga content increases. When the cathodic voltage of -1.2 V_{RHE} is applied, the intensity of the Fourier transform (FT) signal increases in all samples, which indicates that some form of structural change accompanies the CO₂RR in all cases. The extent of absolute change in EXAFS intensity is highest (when viewed from the Cu K-edge) for Cu NPs, and follows the trend CuGa17 ≥ CuGa4 > CuGa37 for the CuGa NPs when looking at both the Cu and the Ga K-edge EXAFS data. As the coordination numbers and disorder are highly correlated, the source of these changes is best captured by the correlation maps, that relate the Debye-Waller Factor (DWF, Å²), with either the first shell *fcc* interatomic distance (*d*, Å) or the first shell *fcc* coordination number (N1) (**Figures S21-S29**). **Table 1** reports the most probable range of values for Cu and Ga extracted from these maps, derived from explicit analysis using EXCURV.³⁷ The most pronounced shifts are observed in the pure Cu NPs, from the perspective of the Cu K-edge, and in the CuGa17 case, with regards to the Ga K-edge. In the case of Cu NPs, such shifts might be linked to the dramatic reconstruction of the NPs (**Figure 4**) and to the reduction of any copper surface oxide initially present leading to a higher net order in the reduced copper phase that remains post CO₂RR (**Figure S24**). However, as no major change in size and/or morphology occurs for the CuGa NPs (**Figures 4**), we attribute the shifts in the values of DWF, *d* and N1 in the correlation maps exclusively to an increase in the overall (static and dynamic) order of the bulk of the crystallites and, in the case of CuGa17, the formation of an alloy with more uniform Ga distribution within the NPs under the operation conditions (**Figures S25-29**).

Interestingly, the d values calculated for Cu and Ga converge towards each other in CuGa17 but not in CuGa37 during CO₂RR. This observation may serve as an indication that Ga tends to rearrange and occupy the crystal sites allowing more uniform distribution of the elements within one NP in CuGa17 NPs; instead, Cu and Ga are less uniformly distributed in CuGa37 during CO₂RR, in agreement with the surface spatial segregation observed in the STEM-EDXS images (Figures 5, S12). This unique behavior of the CuGa37 might be related to its crystal structure, which is distorted and distinctly different from the Cu *fcc*. We hypothesize that such structure might reconstruct more easily than the *fcc* lattice, which is confirmed by molecular dynamics simulations (Figure S30).

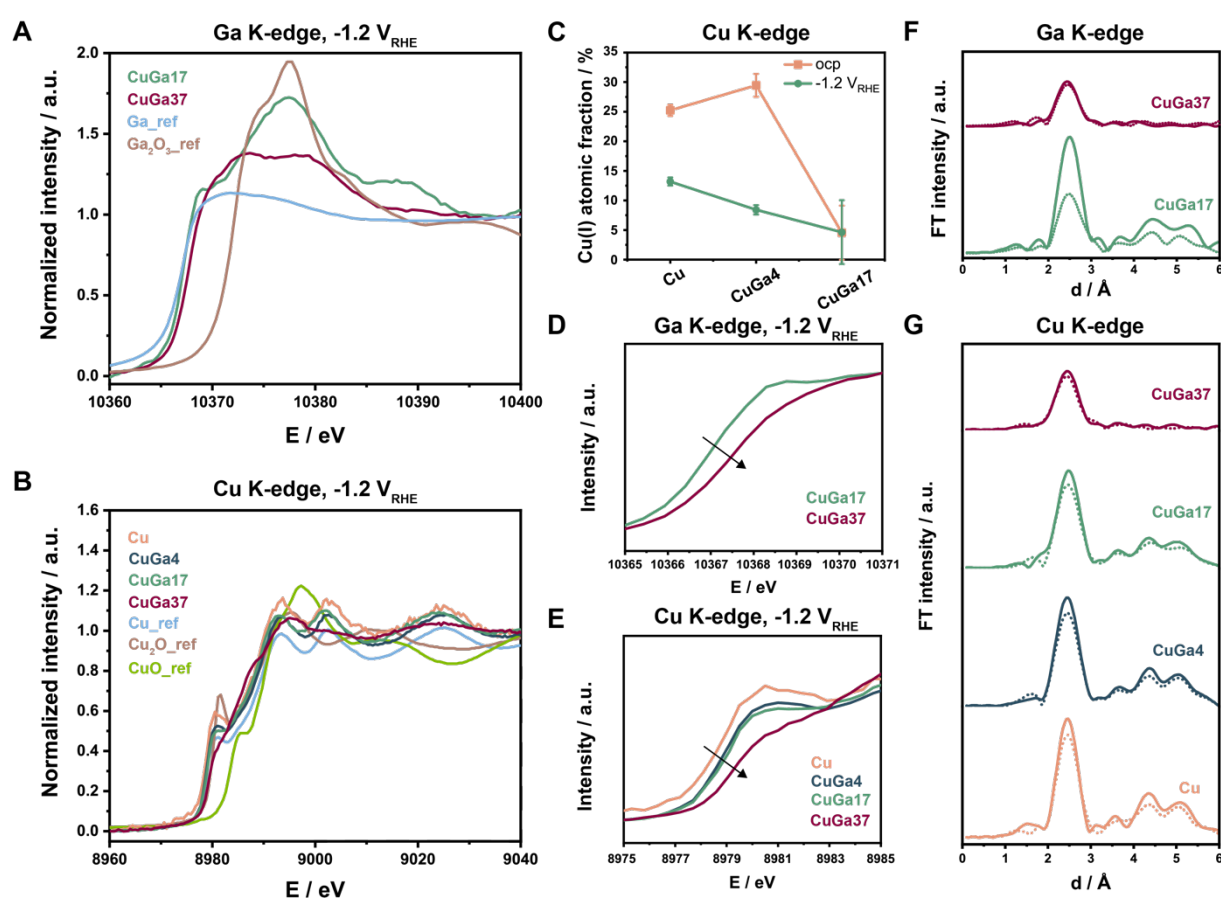


Figure 7. Operando X-Ray spectroscopy during CO₂RR. (A) XANES profiles of Ga K-edge for CuGa17, CuGa37 NPs and the standard samples *operando* at -1.2 V_{RHE}. (B) XANES profiles of Cu K-edge for Cu, CuGa4, CuGa17 and CuGa37 NPs and the standard samples *operando* at -1.2 V_{RHE}. (C) Atomic fraction of Cu¹⁺ obtained from LCA for Cu, CuGa4 and CuGa17 NPs at ocp and *operando* at -1.2 V_{RHE}. (D) Zoomed-in XANES of Ga K-edge for CuGa17 and CuGa37 NPs at *operando* conditions at -1.2 V_{RHE}. (E) Zoomed-in XANES of Cu K-edge for Cu, CuGa4, CuGa17 and CuGa37 NPs at *operando* conditions at -1.2 V_{RHE}. (E)

EXAFS profiles of the Ga shell for Cu, CuGa4, CuGa17 and CuGa37 NPs at ocp (dot line) and *operando* at -1.2 V_{RHE} (solid line). (F) EXAFS profiles of the Cu shell for Cu, CuGa4, CuGa17 and CuGa37 NPs at ocp (dot line) and *operando* at -1.2 V_{RHE} (solid line). The reference samples are bulk materials and were measured *ex situ*. Panels (A), (B), (D) and (E) report the normalized intensities.

Table 1. Structural data extracted from analysis of Cu K-edge and Ga K-edge EXAFS at ocp and *operando* at -1.2 V_{RHE}. These value ranges were extracted from the correlations maps reported in **Figures S24 – S29**.

Sample	N1 (Cu)	N1 (Ga)	d, Å (Cu)	d, Å (Ga)	DWF (2σ ²), Å ² (Cu)	DWF (2σ ²), Å ² (Ga)
Cu ocp	8.5 - 11		2.537		0.012 - 0.017	
Cu -1.2 V _{RHE}	10 - 12		2.519		0.010 - 0.015	
CuGa4 ocp	8 -12		2.533		0.015 - 0.020	
CuGa4 -1.2 V _{RHE}	8 - 12		2.536		0.014 - 0.018	
CuGa17 ocp	8 - 12	9.5 - 12	2.556	2.574	0.016 - 0.022	0.016 - 0.022
CuGa17 -1.2 V _{RHE}	8 - 12	11 - 12	2.562	2.567	0.014 - 0.020	0.007 - 0.012
CuGa37 ocp	6 - 10	6 - 8	2.535	2.523	0.018 - 0.027	0.012 - 0.020
CuGa37 -1.2 V _{RHE}	6 - 10	7 - 10	2.542	2.529	0.017 - 0.024	0.014 - 0.022

Mechanism of stability enhancement in CuGa NPs

With the evidence provided by STEM-EDXS, XPS and *operando* XAS, we rationalize the observations made in this study as it follows and report a summary in **Figure 8**.

First, the pristine 40 nm Cu NPs, which are the reference sample, reconstruct into hollow structures and smaller particles are observed on the electrode (**Figure 4**), which is consistent with previous studies on particles with comparable size.^{5,6,8} These changes are driven by the dissolution/reprecipitation of Cu surface oxide forming at ocp and continue during CO₂RR following the same mechanism via soluble transient species.^{5,6,8} These morphological changes result into the degradation of the catalytic performance with the CO₂RR current density dropping to zero after *ca.* 2 hours (**Figure 3**).

When it comes to CuGa alloy NPs, STEM-EDXS images evidence that morphological changes are significantly suppressed with the addition of Ga (**Figures 4, 5**). Concomitantly, the CO₂RR current is much more stable over time following a trend of CuGa17 > CuGa4 >

CuGa37 (**Figure 3**). XPS and operando XAS data indicate that Ga suppresses Cu oxidation at ocp (**Figures 6, 7**). We further confirm this observation with ICP-MS, which proves that less Cu dissolves at ocp in the case of CuGa17 and CuGa37 compared to the pristine Cu NPs (**Table S2**). Additionally, XPS and *operando* XAS point to significant electronic interactions between Ga and Cu which increase the electron binding energies of both elements within the CuGa NPs. This observation suggests that the alloying lowers the system energy and makes the bond stronger, which agrees well with the fact that the Cu – Ga bond energy (216 kJ/mol) is significantly greater than Cu – Cu (201 kJ/mol) or Ga – Ga (106 kJ/mol).²⁶ Furthermore, the lower electronegativity of Ga indicate that electron density might shift from Ga towards Cu atoms.²⁷ Bader charge calculations for the CuGa alloys propose the same outcome, with higher Ga content resulting in larger charge localized on Cu atoms (**Figure S31**). Actually, the presence of an electron rich Cu correlates well with CH₄ evolution, as recent literature has suggested the presence of an electron poor Cu^{δ+} to be critical to the promotion of the C-C coupling.^{52–54} Overall, the more electron rich Cu and stronger bonds within the alloys compared to the pristine Cu NPs hinder Cu oxidation, and thus dissolution, at ocp and the subsequent reconstruction of the NPs during operation via dissolution mediated by transient soluble intermediates. As for the stability trend observed within the CuGa samples, we should consider that CuGa4 has very little Ga amount within the alloy (*ca.* 1 % during operation), so the performance loss is slower but eventually takes place. CuGa37 has a structure which is intrinsically more distorted and prone to reconstruction (**Figure S30**).^{36,37} Eventually, Cu is re-exposed on the surface (**Figure 5**), which might explain the faster performance degradation compared to the CuGa4 and CuGa17. Considering all the factors coming into play, CuGa17 emerges as the most efficient in preserving the CO₂RR performance.

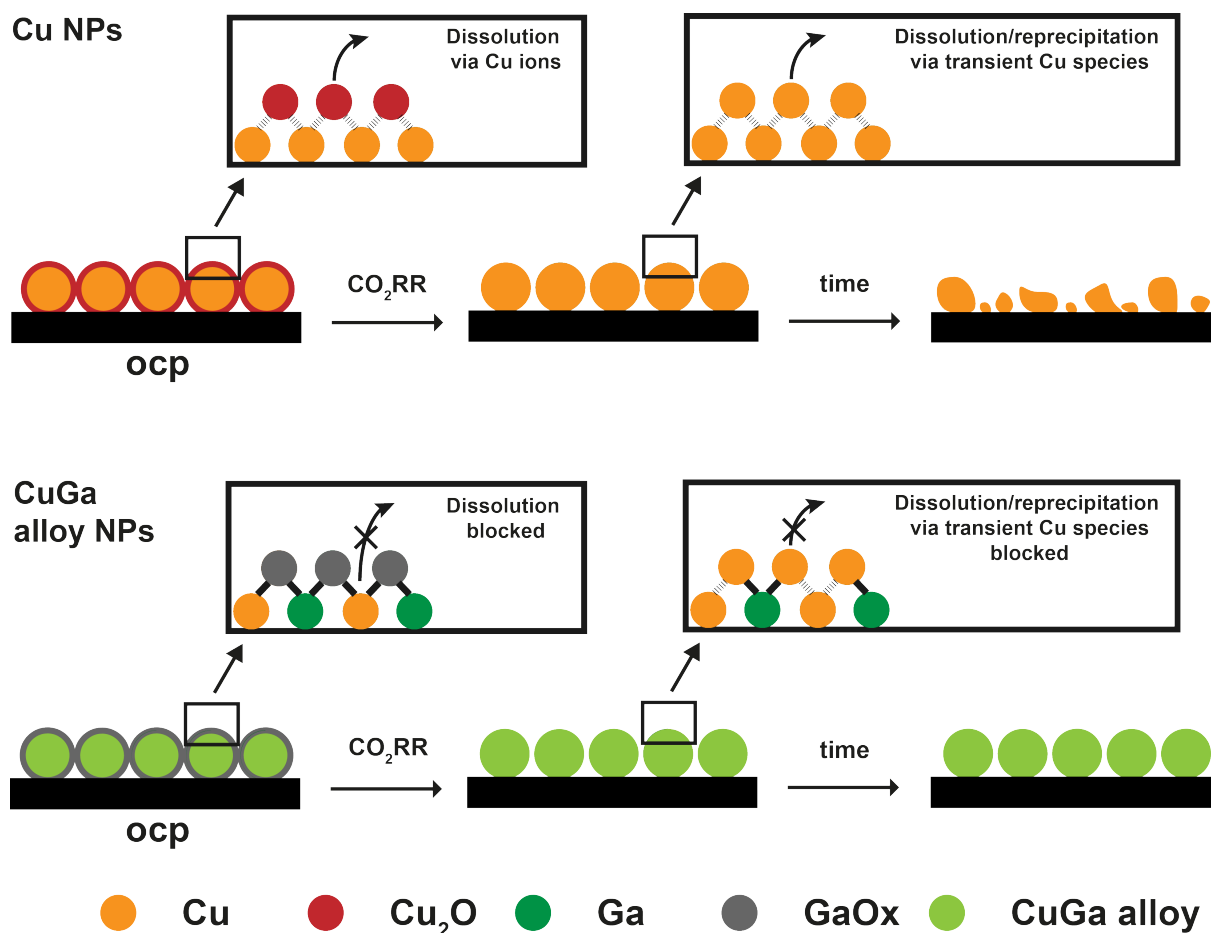


Figure 8. Illustration of the CO_2RR stabilization mechanism in CuGa alloy NPs compared to Cu NPs.

CONCLUSIONS

We have demonstrated that alloying Ga into Cu greatly enhance the stability of the NPs under the reducing conditions of CO_2RR . Compared to the parent Cu NPs, which deactivate rapidly (< 2 h), the addition of Ga results in NPs that do not degrade over extended period of time (up to 20 h). Using a variety of experimental (*ex situ* and *operando*) and theoretical tools we have constructed a framework to rationalize this observation based on the current knowledge on the reconstruction mechanism of Cu NPs during CO_2RR .

We believe that this work can inspire further development of alloyed Cu-based CO_2RR nanocatalysts which are inherently stable during CO_2RR or under other reducing reaction environments. We envision that the metals which have higher oxophilicity and strong M – Cu bonding energies (e.g., early 3d metals, e.g. Sc, Ti, and *p*-group metals, e.g. Al, In, Bi) to have

similar mechanism of hindering Cu reconstruction while driving CO₂RR towards different products of interest and, in general, generating more stable NPs.

ACKNOWLEDGEMENTS

This work was primarily financed by the Swiss National Science Foundation (SNSF) for financial support from grant number 200021L_191997/1. The authors thank the European Synchrotron Radiation Facility in Grenoble, France, for the provision of synchrotron radiation beam time at the Swiss-Norwegian beamline BM31, and Petru Albertini and Dr. Wouter van Beek for assistance. Dr. Natalia Gasilova, Kimoon Lee and Petru Albertini, Dr. Min Wang are acknowledged for ICP-MS, ICP-OES and HPLC measurements.

REFERENCES

- (1) Nitopi, S.; Bertheussen, E.; Scott, S. B.; Liu, X.; Engstfeld, A. K.; Horch, S.; Seger, B.; Stephens, I. E. L.; Chan, K.; Hahn, C.; Nørskov, J. K.; Jaramillo, T. F.; Chorkendorff, I. Progress and Perspectives of Electrochemical CO₂ Reduction on Copper in Aqueous Electrolyte. *Chem. Rev.* **2019**, *119*, 7610–7672.
- (2) Zaza, L.; Rossi, K.; Buonsanti, R. Well-Defined Copper-Based Nanocatalysts for Selective Electrochemical Reduction of CO₂ to C₂ Products. *ACS Energy Lett.* **2022**, *7*, 1284–1291.
- (3) Iyengar, P.; Kolb, M. J.; Pankhurst, J. R.; Calle-Vallejo, F.; Buonsanti, R. Elucidating the Facet-Dependent Selectivity for CO₂ Electroreduction to Ethanol of Cu-Ag Tandem Catalysts. *ACS Catal.* **2021**, *11*, 4456–4463.
- (4) Popović, S.; Smiljanić, M.; Jovanović, P.; Vavra, J.; Buonsanti, R.; Hodnik, N. Stability and Degradation Mechanisms of Copper-Based Catalysts for Electrochemical CO₂ Reduction. *Angew. Chemie Int. Ed.* **2020**, *59*, 14736–14746.
- (5) Huang, J.; Hörmann, N.; Oveisi, E.; Loiudice, A.; De Gregorio, G. L.; Andreussi, O.; Marzari, N.; Buonsanti, R. Potential-Induced Nanoclustering of Metallic Catalysts during Electrochemical CO₂ Reduction. *Nat. Commun.* **2018**, *9*, 3117.
- (6) Möller, T.; Scholten, F.; Thanh, T. N.; Sinev, I.; Timoshenko, J.; Wang, X.; Jovanov, Z.; Gliach, M.; Roldan Cuenya, B.; Varela, A. S.; Strasser, P. Electrocatalytic CO₂ Reduction on CuO_x Nanocubes: Tracking the Evolution of Chemical State, Geometric Structure, and Catalytic Selectivity Using Operando Spectroscopy. *Angew. Chemie Int. Ed.* **2020**, *59*, 17974–17983.

- (7) Kim, D.; Kley, C. S.; Li, Y.; Yang, P. Copper Nanoparticle Ensembles for Selective Electroreduction of CO₂ to C₂–C₃ Products. *Proc. Natl. Acad. Sci. U. S. A.* **2017**, *114*, 10560–10565.
- (8) Vavra, J.; Shen, T.-H.; Stoian, D.; Tileli, V.; Buonsanti, R. Real-time Monitoring Reveals Dissolution/Redeposition Mechanism in Cu Nanocatalysts during the Initial Stages of the CO₂ Reduction Reaction. *Angew. Chemie Int. Ed.* **2021**, *60*, 1347–1354.
- (9) Yoo, J. M.; Shin, H.; Chung, D. Y.; Sung, Y. E. Carbon Shell on Active Nanocatalyst for Stable Electrocatalysis. *Acc. Chem. Res.* **2022**, *55*, 1278–1289.
- (10) Chung, D. Y.; Jun, S. W.; Yoon, G.; Kwon, S. G.; Shin, D. Y.; Seo, P.; Yoo, J. M.; Shin, H.; Chung, Y.-H.; Kim, H.; Mun, B. S.; Lee, K.-S.; Lee, N.-S.; Yoo, S. J.; Lim, D.-H.; Kang, K.; Sung, Y.-E.; Hyeon, T. Highly Durable and Active PtFe Nanocatalyst for Electrochemical Oxygen Reduction Reaction. *J. Am. Chem. Soc.* **2015**, *137*, 15478–15485.
- (11) Li, Y.; Cui, F.; Ross, M. B.; Kim, D.; Sun, Y.; Yang, P. Structure-Sensitive CO₂ Electroreduction to Hydrocarbons on Ultrathin 5-Fold Twinned Copper Nanowires. *Nano Lett.* **2017**, *17*, 1312–1317.
- (12) Zhang, J.; Sasaki, K.; Sutter, E.; Adzic, R. R. Stabilization of Platinum Oxygen-Reduction Electrocatalysts Using Gold Clusters. *Science* **2007**, *315*, 220–222.
- (13) Zhang, J.; Xu, W.; Liu, Y.; Hung, S. F.; Liu, W.; Lam, Z.; Tao, H. B.; Yang, H.; Cai, W.; Xiao, H.; Chen, H.; Liu, B. In Situ Precise Tuning of Bimetallic Electronic Effect for Boosting Oxygen Reduction Catalysis. *Nano Lett.* **2021**, *21*, 7753–7760.
- (14) Jong Yoo, S.; Kim, S. K.; Jeon, T. Y.; Jun Hwang, S.; Lee, J. G.; Lee, S. C.; Lee, K. S.; Cho, Y. H.; Sung, Y. E.; Lim, T. H. Enhanced Stability and Activity of Pt–Y Alloy Catalysts for Electrocatalytic Oxygen Reduction. *Chem. Commun.* **2011**, *47*, 11414–11416.
- (15) Lv, F.; Feng, J.; Wang, K.; Dou, Z.; Zhang, W.; Zhou, J.; Yang, C.; Luo, M.; Yang, Y.; Li, Y.; Gao, P.; Guo, S. Iridium-Tungsten Alloy Nanodendrites as pH-Universal Water-Splitting Electrocatalysts. *ACS Cent. Sci.* **2018**, *4*, 1244–1252.
- (16) Lončar, A.; Escalera-López, D.; Ruiz-Zepeda, F.; Hrnjić, A.; Šala, M.; Jovanović, P.; Bele, M.; Cherevko, S.; Hodnik, N. Sacrificial Cu Layer Mediated the Formation of an Active and Stable Supported Iridium Oxygen Evolution Reaction Electrocatalyst. *ACS Catal.* **2021**, *11*, 12510–12519.
- (17) Đukić, T.; Moriau, L. J.; Pavko, L.; Kostelec, M.; Prokop, M.; Ruiz-Zepeda, F.; Šala, M.; Dražić, G.; Gatalo, M.; Hodnik, N. Understanding the Crucial Significance of the

- Temperature and Potential Window on the Stability of Carbon Supported Pt-Alloy Nanoparticles as Oxygen Reduction Reaction Electrocatalysts. *ACS Catal.* **2022**, *12*, 101–115.
- (18) Cheng, H.; Gui, R.; Yu, H.; Wang, C.; Liu, S.; Liu, H.; Zhou, T.; Zhang, N.; Zheng, X.; Chu, W.; Lin, Y.; Wu, H. A.; Wu, C.; Xie, Y. Subsize Pt-Based Intermetallic Compound Enables Long-Term Cyclic Mass Activity for Fuel-Cell Oxygen Reduction. *Proc. Natl. Acad. Sci. U. S. A.* **2021**, *118*, e2104026118.
- (19) Ma, S.; Sadakiyo, M.; Heim, M.; Luo, R.; Haasch, R. T.; Gold, J. I.; Yamauchi, M.; Kenis, P. J. A. Electroreduction of Carbon Dioxide to Hydrocarbons Using Bimetallic Cu-Pd Catalysts with Different Mixing Patterns. *J. Am. Chem. Soc.* **2017**, *139*, 47–50.
- (20) Castilla-Amorós, L.; Schouwink, P.; Oveisi, E.; Okatenko, V.; Buonsanti, R. Tailoring Morphology and Elemental Distribution of Cu-In Nanocrystals via Galvanic Replacement. *J. Am. Chem. Soc.* **2022**, *144*, 42.
- (21) Kim, D.; Resasco, J.; Yu, Y.; Asiri, A. M.; Yang, P. Synergistic Geometric and Electronic Effects for Electrochemical Reduction of Carbon Dioxide Using Gold–Copper Bimetallic Nanoparticles. *Nat. Commun.* **2014**, *5*, 4948.
- (22) Kim, D.; Xie, C.; Becknell, N.; Yu, Y.; Karamad, M.; Chan, K.; Crumlin, E. J.; Nørskov, J. K.; Yang, P. Electrochemical Activation of CO₂ through Atomic Ordering Transformations of AuCu Nanoparticles. *J. Am. Chem. Soc.* **2017**, *139*, 8329–8336.
- (23) Yin, Z.; Gao, D.; Yao, S.; Zhao, B.; Cai, F.; Lin, L.; Tang, P.; Zhai, P.; Wang, G.; Ma, D.; Bao, X. Highly Selective Palladium-Copper Bimetallic Electrocatalysts for the Electrochemical Reduction of CO₂ to CO. *Nano Energy* **2016**, *27*, 35–43.
- (24) Tran, K.; Ulissi, Z. W. Active Learning across Intermetallics to Guide Discovery of Electrocatalysts for CO₂ Reduction and H₂ Evolution. *Nat. Catal.* **2018**, *1*, 696–703.
- (25) Zhong, M.; Tran, K.; Min, Y.; Wang, C.; Wang, Z.; Dinh, C. T.; De Luna, P.; Yu, Z.; Rasouli, A. S.; Brodersen, P.; Sun, S.; Voznyy, O.; Tan, C. S.; Askerka, M.; Che, F.; Liu, M.; Seifitokaldani, A.; Pang, Y.; Lo, S. C.; Ip, A.; Ulissi, Z.; Sargent, E. H. Accelerated Discovery of CO₂ Electrocatalysts Using Active Machine Learning. *Nature* **2020**, *581*, 178–183.
- (26) Luo, Y. R. *Comprehensive Handbook of Chemical Bond Energies*, 1st Editio.; Luo, Y. R., Ed.; CRC Press: Boca Raton, FL, 2007.
- (27) Boeyens, J. C. A. The Periodic Electronegativity Table. *Zeitschrift für Naturforsch. - Sect. B J. Chem. Sci.* **2008**, *63*, 199–209.
- (28) Loiudice, A.; Lobaccaro, P.; Kamali, E. A.; Thao, T.; Huang, B. H.; Ager, J. W.;

- Buonsanti, R. Tailoring Copper Nanocrystals towards C₂ Products in Electrochemical CO₂ Reduction. *Angew. Chemie Int. Ed.* **2016**, *55*, 5789–5792.
- (29) Clarysse, J.; Moser, A.; Yarema, O.; Wood, V.; Yarema, M. Size- and Composition-Controlled Intermetallic Nanocrystals via Amalgamation Seeded Growth. *Sci. Adv.* **2021**, *7*, eabg1934.
- (30) Van Beek, W.; Safonova, O. V.; Wiker, G.; Emerich, H. SNBL, a Dedicated Beamline for Combined in Situ X-Ray Diffraction, X-Ray Absorption and Raman Scattering Experiments. *Phase Transitions* **2011**, *84*, 726–732.
- (31) Okatenko, V.; Castilla-Amorós, L.; Stoian, D. C.; Vávra, J.; Loiudice, A.; Buonsanti, R. The Native Oxide Skin of Liquid Metal Ga Nanoparticles Prevents Their Rapid Coalescence during Electrocatalysis. *J. Am. Chem. Soc.* **2022**, *144*, 10053–10063.
- (32) Varandili, S. B.; Stoian, D.; Vavra, J.; Rossi, K.; Pankhurst, J. R.; Guntern, Y. T.; López, N.; Buonsanti, R. Elucidating the Structure-Dependent Selectivity of CuZn towards Methane and Ethanol in CO₂ Electroreduction Using Tailored Cu/ZnO Precatalysts. *Chem. Sci.* **2021**, *12*, 14484–14493.
- (33) Ravel, B.; Newville, M. ATHENA, ARTEMIS, HEPHAESTUS: Data Analysis for X-Ray Absorption Spectroscopy Using IFEFFIT. *J. Synchrotron Radiat.* **2005**, *12*, 537–541.
- (34) Figueroa, S. J. A.; Prestipino, C. PrestoPronto: A Code Devoted to Handling Large Data Sets. *J. Phys. Conf. Ser.* **2016**, *712*, 012012.
- (35) Binsted, N. EXCURV98, CCLRC Daresbury Laboratory Computer Program. CCLRC Daresbury Laboratory: Daresbury 1998.
- (36) Li, J. B.; Ji, L. N.; Liang, J. K.; Zhang, Y.; Luo, J.; Li, C. R.; Rao, G. H. A Thermodynamic Assessment of the Copper–Gallium System. *Calphad* **2008**, *32*, 447–453.
- (37) Stokhuyzen, R.; Brandon, J. K.; Chieh, P. C.; Pearson, W. B. Copper–Gallium, Γ1-Cu₉Ga₄. *Acta Crystallogr. Sect. B* **1974**, *30*, 2910–2911.
- (38) Bagchi, D.; Raj, J.; Kumar Singh, A.; Cherevotan, A.; Roy, S.; Manoj, K. S.; Vinod, C. P.; Peter, S. C. Structure-Tailored Surface Oxide on Cu-Ga Intermetallics Enhances CO₂ Reduction Selectivity to Methanol at Ultra-Low Potential. *Adv. Mater.* **2022**, *12*, 2109426.
- (39) Wang, Z.; Yuan, Q.; Shan, J.; Jiang, Z.; Xu, P.; Hu, Y.; Zhou, J.; Wu, L.; Niu, Z.; Sun, J.; Cheng, T.; William A. Goddard, I. Highly Selective Electrocatalytic Reduction of CO₂ into Methane on Cu–Bi Nanoalloys. *J. Phys. Chem. Lett.* **2020**, *11*, 7261–7266.

- (40) Jeon, H. S.; Sinev, I.; Scholten, F.; Divins, N. J.; Zegkinoglou, I.; Pielsticker, L.; Roldan Cuenya, B. Operando Evolution of the Structure and Oxidation State of Size-Controlled Zn Nanoparticles during CO₂ Electroreduction. *J. Am. Chem. Soc.* **2018**, *140*, 9383–9386.
- (41) Cheng, T.; Xiao, H.; Goddard, W. A. Free-Energy Barriers and Reaction Mechanisms for the Electrochemical Reduction of CO on the Cu(100) Surface, Including Multiple Layers of Explicit Solvent at PH 0. *J. Phys. Chem. Lett.* **2015**, *6*, 4767–4773.
- (42) Peterson, A. A.; Abild-Pedersen, F.; Studt, F.; Rossmeisl, J.; Nørskov, J. K. How Copper Catalyzes the Electroreduction of Carbon Dioxide into Hydrocarbon Fuels. *Energy Environ. Sci.* **2010**, *3*, 1311–1315.
- (43) Hori, Y.; Wakebe, H.; Tsukamoto, T.; Koga, O. Electrocatalytic Process of CO Selectivity in Electrochemical Reduction of CO₂ at Metal Electrodes in Aqueous Media. *Electrochim. Acta* **1994**, *39*, 1833–1839.
- (44) Ross, M. B.; Dinh, C. T.; Li, Y.; Kim, D.; De Luna, P.; Sargent, E. H.; Yang, P. Tunable Cu Enrichment Enables Designer Syngas Electrosynthesis from CO₂. *J. Am. Chem. Soc.* **2017**, *139*, 9359–9363.
- (45) Cui, C.; Gan, L.; Heggen, M.; Rudi, S.; Strasser, P. Compositional Segregation in Shaped Pt Alloy Nanoparticles and Their Structural Behaviour during Electrocatalysis. *Nat. Mater.* **2013**, *12*, 765–771.
- (46) Cademartiri, L.; Thuo, M. M.; Nijhuis, C. A.; Reus, W. F.; Tricard, S.; Barber, J. R.; Sodhi, R. N. S.; Brodersen, P.; Kim, C.; Chiechi, R. C.; Whitesides, G. M. Electrical Resistance of Ag^{TS}-S(CH₂)_{n-1}CH₃//Ga₂O₃/EGaIn Tunneling Junctions. *J. Phys. Chem. C* **2012**, *116*, 10848–10860.
- (47) Farrell, Z. J.; Tabor, C. Control of Gallium Oxide Growth on Liquid Metal Eutectic Gallium/Indium Nanoparticles via Thiolation. *Langmuir* **2018**, *34*, 234–240.
- (48) Castilla-Amorós, L.; Chien, T. C. C.; Pankhurst, J. R.; Buonsanti, R. Modulating the Reactivity of Liquid Ga Nanoparticle Inks by Modifying Their Surface Chemistry. *J. Am. Chem. Soc.* **2022**, *144*, 1993–2001.
- (49) Biesinger, M. C. Advanced Analysis of Copper X-Ray Photoelectron Spectra. *Surf. Interface Anal.* **2017**, *49*, 1325–1334.
- (50) Bourque, J. L.; Biesinger, M. C.; Baines, K. M. Chemical State Determination of Molecular Gallium Compounds Using XPS. *Dalt. Trans.* **2016**, *45*, 7678–7696.
- (51) Lee, S. H.; Lin, J. C.; Farmand, M.; Landers, A. T.; Feaster, J. T.; Avilés Acosta, J. E.; Beeman, J. W.; Ye, Y.; Yano, J.; Mehta, A.; Davis, R. C.; Jaramillo, T. F.; Hahn, C.;

- Drisdell, W. S. Oxidation State and Surface Reconstruction of Cu under CO₂ Reduction Conditions from in Situ X-Ray Characterization. *J. Am. Chem. Soc.* **2021**, *143*, 588–592.
- (52) Gao, D.; Sinev, I.; Scholten, F.; Arán-Ais, R. M.; Divins, N. J.; Kvashnina, K.; Timoshenko, J.; Roldan Cuenya, B. Selective CO₂ Electroreduction to Ethylene and Multicarbon Alcohols via Electrolyte-Driven Nanostructuring. *Angew. Chemie Int. Ed.* **2019**, *58*, 17047–17053.
- (53) Yang, P. P.; Zhang, X. L.; Gao, F. Y.; Zheng, Y. R.; Niu, Z. Z.; Yu, X.; Liu, R.; Wu, Z. Z.; Qin, S.; Chi, L. P.; Duan, Y.; Ma, T.; Zheng, X. S.; Zhu, J. F.; Wang, H. J.; Gao, M. R.; Yu, S. H. Protecting Copper Oxidation State via Intermediate Confinement for Selective CO₂ Electroreduction to C₂₊ Fuels. *J. Am. Chem. Soc.* **2020**, *142*, 6400–6408.
- (54) Chou, T. C.; Chang, C. C.; Yu, H. L.; Yu, W. Y.; Dong, C. L.; Velasco-Vélez, J. J.; Chuang, C. H.; Chen, L. C.; Lee, J. F.; Chen, J. M.; Wu, H. L. Controlling the Oxidation State of the Cu Electrode and Reaction Intermediates for Electrochemical CO₂ Reduction to Ethylene. *J. Am. Chem. Soc.* **2020**, *142*, 2857–2867.